CANCER

Engineered probiotics for local tumor delivery of checkpoint blockade nanobodies

Candice R. Gurbatri[1], Ioana Lia[1], Rosa Vincent[1], Courtney Coker[1], Samuel Castro[1], Piper M. Treuting[2], Taylor E. Hinchliffe[1], Nicholas Arpaia[3,4], Tal Danino[1,4,5]*

Checkpoint inhibitors have revolutionized cancer therapy but only work in a subset of patients and can lead to a multitude of toxicities, suggesting the need for more targeted delivery systems. Because of their preferential colonization of tumors, microbes are a natural platform for the local delivery of cancer therapeutics. Here, we engineer a probiotic bacteria system for the controlled production and intratumoral release of nanobodies targeting programmed cell death–ligand 1 (PD-L1) and cytotoxic T lymphocyte–associated protein-4 (CTLA-4) using a stabilized lysing release mechanism. We used computational modeling coupled with experimental validation of lysis circuit dynamics to determine the optimal genetic circuit parameters for maximal therapeutic efficacy. A single injection of this engineered system demonstrated an enhanced therapeutic response compared to analogous clinically relevant antibodies, resulting in tumor regression in syngeneic mouse models. Supporting the potentiation of a systemic immune response, we observed a relative increase in activated T cells, an abscopal effect, and corresponding increases in systemic T cell memory populations in mice treated with probiotically delivered checkpoint inhibitors. Last, we leveraged the modularity of our platform to achieve enhanced therapeutic efficacy in a poorly immunogenic syngeneic mouse model through effective combinations with a probiotically produced cytokine, granulocyte-macrophage colony-stimulating factor (GM-CSF). Together, these results demonstrate that our engineered probiotic system bridges synthetic biology and immunology to improve upon checkpoint blockade delivery.

INTRODUCTION

Immune checkpoint inhibitors targeting programmed cell death–ligand 1 (PD-L1) and cytotoxic T lymphocyte–associated protein-4 (CTLA-4) have revolutionized the paradigm of cancer immunotherapy treatments, achieving tumor regression in several cancers (1, 2). However, they can also result in immune-related adverse effects, with up to 70% of patients experiencing measurable toxicity such as fatigue, skin rashes, endocrine disorders, or hepatic toxicities (3–6). Furthermore, although combination therapies of anti–PD-L1/PD-1 and anti–CTLA-4 monoclonal antibodies (mAbs) are more efficacious than single therapy regimens, combined checkpoint blockade therapy causes higher-grade toxicity, leading to the favoring of less efficacious monotherapies or eventual drug discontinuation (7, 8). Thus, there is a clear need for the improved delivery of immune checkpoint inhibitors to circumvent these limitations and to provide a more localized, sustained, and minimally invasive therapeutic option.

The rapid development of genetic technologies has enabled the engineering of intelligent microbial delivery systems for therapeutic applications. Specifically, synthetic biology has generated numerous examples of genetic circuits controlling bacteria growth and gene expression (9–16), allowing them to sense and respond to disease states of inflammation, infection, and cancer (17–20). Particularly for cancer, a multitude of studies has shown that systemic administration of bacteria results in their selective colonization of tumors, providing a convenient opportunity for tumor drug delivery. This occurs primarily due to reduced immune surveillance along with the ability of bacteria to grow within the hypoxic and necrotic tumor core (21–25). At the same time, microbiome research efforts have revealed the widespread prevalence of microbes within malignant tissue that do not cause infections or other long-term detrimental health effects (26, 27). Because bacteria are both inherently present and selectively grow within tumors, they provide a natural platform for the development of programmable therapeutic delivery vehicles.

Harnessing the converging advancements in both immunotherapy and synthetic biology, we engineered probiotic bacteria to locally and controllably release PD-L1 and CTLA-4 antagonists in the form of blocking nanobodies. Specifically, we coupled immunotherapeutic expression to an optimized lysing mechanism such that probiotic bacteria carrying the nanobodies home to the necrotic tumor core, grow to a critical density, and lyse, effectively releasing the therapeutics continuously within the tumor microenvironment (TME; Fig. 1A).

RESULTS

Design and characterization of probiotically expressed PD-L1 and CTLA-4 nanobodies

A camelid single-domain antibody fragment, or nanobody, blocking PD-L1 or CTLA-4 was chosen from the Research Collaboratory for Structural Bioinformatics Protein Data Bank (RCSB PDB) as therapeutic cargo. Unlike antibodies with a molecular size of ~150 kDa, nanobodies are typically ~15 kDa and lack an Fc region that requires glycosylation by mammalian cells, allowing them to be recombinantly produced in bacteria (28, 29). Nanobodies provide multiple advantages, including their small size, which allows increased diffusion within the TME, and more rapid clearance from the bloodstream through glomerular filtration, thereby reducing off-target effects (30). Although faster blood clearance may suggest shorter therapeutic

[1]Department of Biomedical Engineering, Columbia University, New York, NY 10027, USA. [2]Department of Comparative Medicine, University of Washington, Seattle, WA 98195, USA. [3]Department of Microbiology & Immunology, Vagelos College of Physicians and Surgeons of Columbia University, New York, NY 10032, USA. [4]Herbert Irving Comprehensive Cancer Center, Columbia University, New York, NY 10027, USA. [5]Data Science Institute, Columbia University, New York, NY 10027, USA.
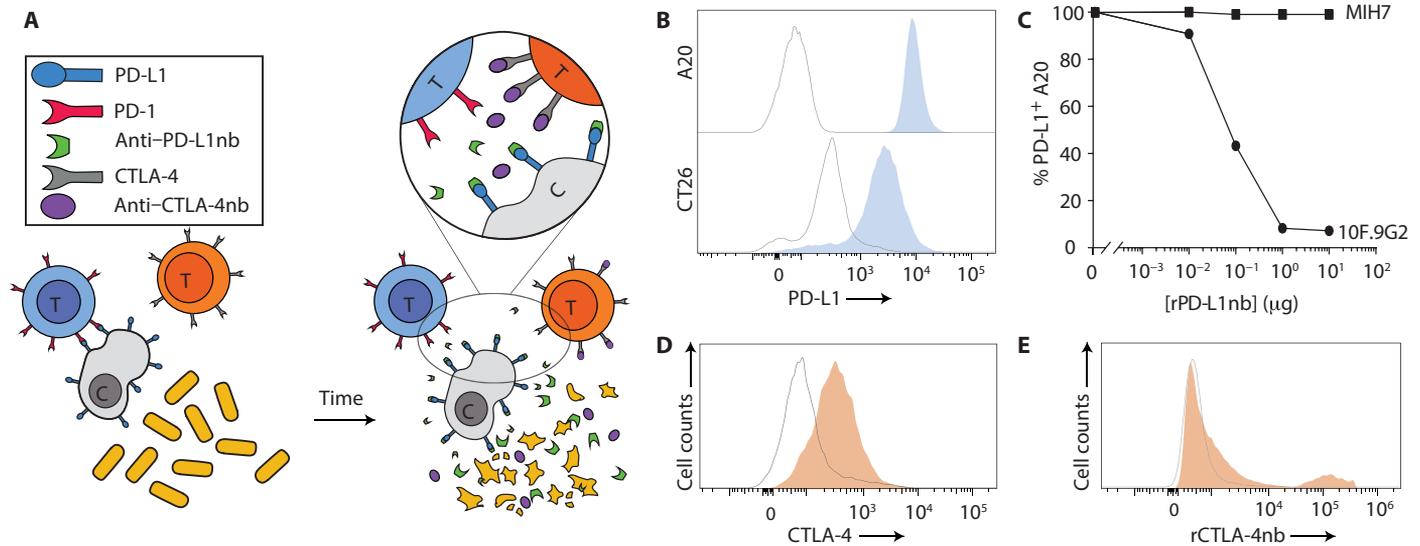*Corresponding author. Email: td2506@columbia.edu

Fig. 1. Design and characterization of a probiotic cancer therapy system for release of functional PD-L1– and CTLA-4–blocking nanobodies. (**A**) Schematic showing the mechanism by which engineered bacteria controllably release constitutively produced PD-L1 and CTLA-4 blocking nanobodies intratumorally. (**B**) Flow cytometric analysis of PD-L1 expression on A20 and CT26 cells (gray, unstained; blue, PD-L1), where the y axis of histograms represents cell counts normalized to mode. (**C**) Binding curves of rPD-L1nb to the 10F.9G2 and MIH7 PD-L1 epitopes on A20 cells. (**D** and **E**) Splenocytes were isolated from healthy C57BL/6 mice and analyzed by flow cytometry for (D) intracellular CTLA-4 expression (gray, unstimulated CD3$^+$ splenocytes; orange, PMA/ionomycin-simulated CD3$^+$ splenocytes), where the y axis of the histogram represents cell counts normalized to mode, and (E) rCTLA-4nb binding to extracellular CTLA-4 (gray, secondary anti-HIS antibody alone gated on CD3$^+$ splenocytes; orange, rCTLA-4nb gated on CD3$^+$ splenocytes), where the y axis of the histogram represents cell counts normalized to mode.

impact, the use of live bacteria as a delivery vehicle allows continuous and intratumoral nanobody production to improve upon this limitation.

We first sought to validate the binding capabilities of nanobodies targeting PD-L1 and CTLA-4. For purification and downstream binding detection purposes, we cloned a 6× histidine residue tag onto both nanobodies (rPD-L1nb and rCTLA-4nb). Using flow cytometry, we then confirmed PD-L1 expression on A20 and CT26 cell lines (Fig. 1B), which have demonstrated modest antitumor responses to checkpoint inhibitor therapies in syngeneic murine models of B cell lymphoma and colorectal carcinoma, respectively (*31, 32*). To examine the binding of the PD-L1nb, dilutions of rPD-L1nb were coincubated with a constant concentration of a fluorescently conjugated anti–PD-L1 mAb specific to epitopes recognized by either the 10F.9G2 or MIH7 clones on PD-L1^{high} A20 cells. By flow cytometry, we observed an increase in the 10F.9G2 mAb fluorescence as the rPD-L1nb concentration was decreased, with ~100 ng of rPD-L1nb binding 50% of the target (Fig. 1C and fig. S1A). However, no change in fluorescence of the MIH7 mAb was observed as a function of rPD-L1nb concentration, suggesting that the rPD-L1nb specifically binds to an epitope similar to that recognized by a 10F.9G2-specific mAb (Fig. 1C). Comparable results were observed using crude bacterial lysate containing the PD-L1nb to ensure that binding was still possible in conditions more similar to those of tumors in vivo (fig. S1, B to D).

To investigate the binding properties of the CTLA-4nb, murine splenocytes were harvested and stimulated with phorbol 12-myristate 13-acetate (PMA)/ionomycin for 48 hours to induce CTLA-4 expression, which was subsequently detected by intracellular staining using a fluorescently conjugated anti–CTLA-4 mAb on T cells (Fig. 1D). We then incubated our recombinantly produced and purified CTLA-4nb with activated splenocytes and probed the cells with a fluorescently conjugated anti-histidine (anti-HIS) mAb to detect the extracellular

binding of the rCTLA-4nb. Using flow cytometry, we identified an anti-HIS signal on stimulated CD3$^+$ splenocytes, suggesting that the rCTLA-4nb is binding to an activated T cell population (Fig. 1E).

After confirming that the nanobodies bound to their respective targets, the PD-L1nb and CTLA-4nb sequences were cloned onto separate plasmids downstream of a strong constitutive *tac* promoter on a high-copy plasmid to allow maximal gene expression (fig. S2A). A human influenza hemagglutinin (HA) protein tag was added to the 3′ end of the nanobody sequences for in vitro visualization, and an Axe/Txe stability mechanism was cloned into the vector to prevent plasmid loss during bacterial replication (*33*). The plasmid was then transformed into the probiotic strain, *Escherichia coli* Nissle 1917, containing a genomically integrated *luxCDABE* cassette for bacterial tracking in vivo (EcN-lux) (*34*). *E. coli* Nissle 1917 was chosen as a therapeutic vehicle for its proven safety, as it is currently prescribed for oral administration in humans, as well as its ease in genetic manipulation for the delivery of cancer therapeutics (*35–37*).

Optimization of the therapeutic release mechanism

We next sought to maximize therapeutic efficacy by optimizing a synchronized lysis circuit whereby a bacterial population lyses once a critical density or quorum is reached, effectively releasing its therapeutic payload (*18*). Such circuits have been shown to aid in tumor-selective bacterial production, population limitation, and periodic therapeutic release, thereby serving multiple purposes critical for translational efforts (*18*). However, one drawback of the original system is its reliance on plasmids, which could lead to recombination, mutations, and plasmid loss during the bacterial growth cycle (*38, 39*). To make this circuit more translationally relevant and stable, the original two-plasmid system was combined into a single operon on a plasmid and subsequently integrated into the genome of EcN-lux. Here, the quorum-sensing *plux* promoter drives transcription

of the quorum-sensing gene, *luxI*, and the phage-derived lysis gene, *φX174E* (Fig. 2A and fig. S2B).

Although genomic integration offers stability, it also reduces the copy number of quorum-sensing genes, prompting us to explore how this reduction would affect therapeutic production. Using a system of ordinary differential equations, we modeled the dynamics of the circuit variants differing in copy number of the *luxI* and *φX174E* genes (see the "Mathematical model" section). We first simulated two quantities: (i) number of bacteria required for the first lysis event and (ii) time required to reach the first lysis event. We observed that decreasing copy number monotonically increased the number of bacteria required, but time to lysis displayed nonmonotonic behavior (Fig. 2B). To further understand how these parameters ultimately influence therapeutic production, we additionally simulated the amount of protein released by the copy number variants over time (Fig. 2C). Together, these simulations suggested that the single-copy variant produces the greatest amount of therapeutic protein across experimentally relevant copy numbers.

To validate our simulations, we built a library of plasmid variants covering a range of copy numbers for the quorum-sensing genes, including a single genomic integration of the operon into the φ80 site of the EcN-lux strain [synchronized lysing integrated circuit (SLIC); Fig. 2A]. Tracking of bacteria concentration over time in 96-well plates suggested that more copies of *luxI* and *φX174E* lead to lysis at a lower bacteria concentration with a rapidly decaying relationship (Fig. 2D and data file S1). Furthermore, lower copy number variants generally required more time to reach a critical density, but the relationship exhibited nonmonotonic behavior, consistent with our simulations (Fig. 2D). To experimentally validate the relationship between copy number and therapeutic production, we transformed each circuit variant plasmid (fig. S2B) and our therapeutic plasmid engineered to constitutively produce superfolder GFP (sfGFP) (fig. S2A) into EcN-lux and tracked fluorescence in a plate reader over time. We observed a pattern similar to our simulations, where the lowest copy number produced the most sfGFP in a given time period compared to higher copy number variants (Fig. 2E). Together,
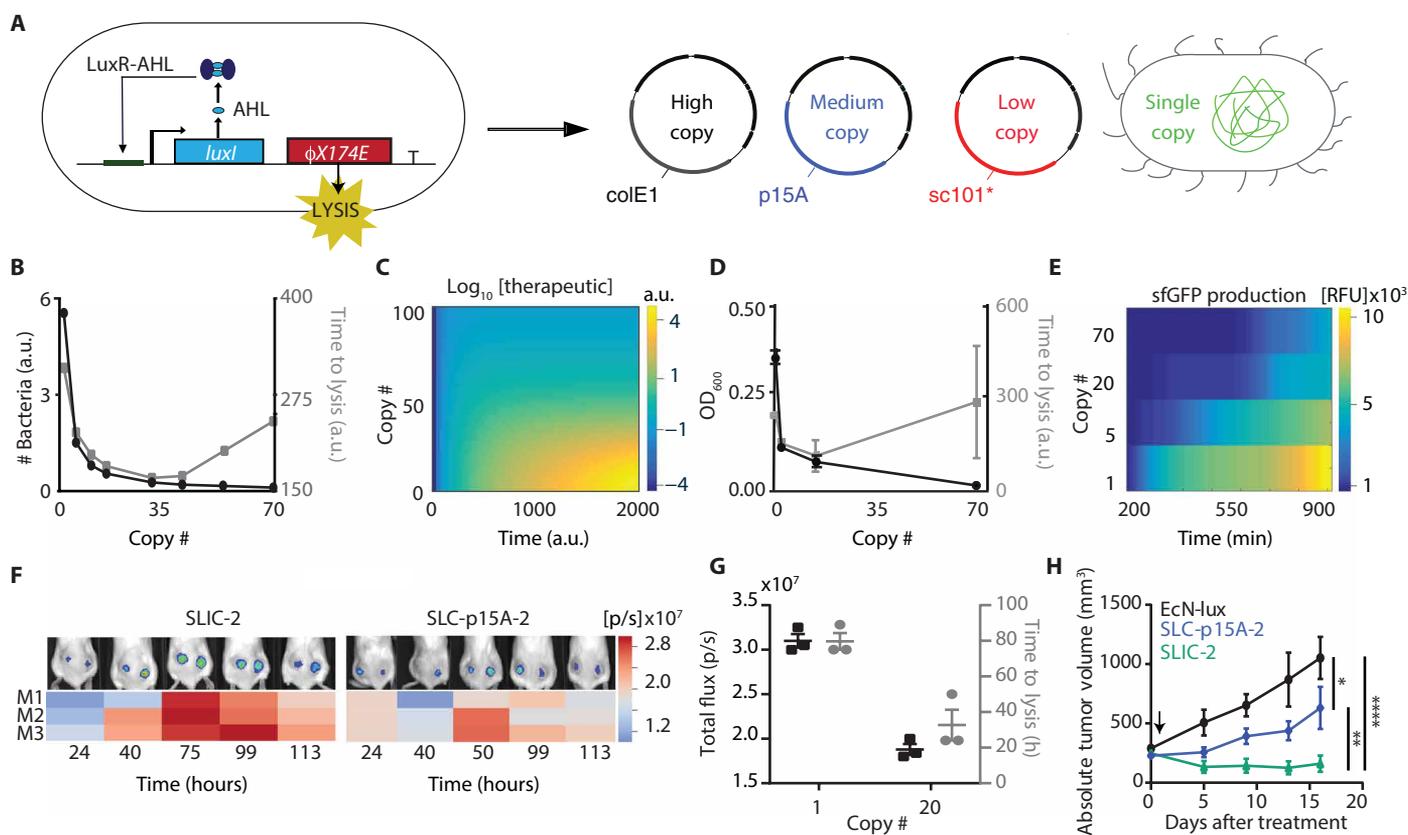

Fig. 2. Characterization of lysis circuit variant dynamics. (**A**) Lysis circuit diagram in which *plux* drives the transcription of *luxI* and *φX174E* genes under a single promoter. The circuit was cloned onto three plasmids with different copy numbers: sc101* (3 to 4 copies, low), p15A (15 to 20 copies, medium), and colE1 (70 to 100 copies, high) and integrated once into the φ80 site of the EcN-lux genome [synchronized lysing integrated circuit (SLIC)]. (**B**) Computational simulation of the number of bacteria required for the first lysis event as a function of copy number (left *y* axis, black) and the time to first lysis event (right *y* axis, gray). a.u., arbitrary units. (**C**) Simulated heatmap of therapeutic protein produced (*z* axis, where the amount produced is represented by the color bar) as a function of copy number (*y* axis) and time (*x* axis). (**D**) Experimental data showing the number of bacteria required for the first lysis event as a function of copy number and time to first lysis event. Data are represented as means ± SEM of three repeated experiments. (**E**) Heatmap of sfGFP produced over time by the copy number variants as quantified by a plate reader. RFU, relative fluorescence units. (**F**) IVIS images showing bioluminescent bacterial populations and heatmaps quantifying the total flux [photons per second (p/s)] of bacterial populations over time for SLIC-2 and SLC-p15A-2 variants. (**G**) Quantification of IVIS images plotting the total flux (black) of SLIC-2 and SLC-p15A-2 variant bacterial populations and time to first lysis event (gray). (**H**) BALB/c mice were implanted subcutaneously with 5×10^6 A20 cells on both hind flanks. When tumors reached ~150 to 200 mm³, mice received one intratumoral injection of EcN-lux, SLIC-2, or SLIC-p15A-2. Graph is of mean absolute tumor trajectories (*n* = 4 to 5 tumors per group; two-way ANOVA with Bonferroni posttest, *P = 0.0172, **P = 0.0033, and ****P < 0.0001; error bars represent SEM of biological replicates). Individual tumor trajectories are shown in fig. S3.

these results suggest that the nonmonotonic behavior is due to a higher amount of basal lysis when high copy numbers of the $\phi X174E$ gene are present, resulting in slower growth, longer time to reach quorum and lysis, and ultimately lower therapeutic production.

We next tested whether the lowest copy number variant, SLIC, and the highest copy number variant with a compatible origin of replication to our high-copy therapeutic plasmid, SLC-p15A, demonstrated lysis behavior and predictable dynamics in vivo. To more accurately replicate a therapeutic setting, we transformed both variants with either the CTLA-4nb– or PD-L1nb–producing plasmid and dosed mice with an equal parts mix of SLIC bacteria expressing nanobodies against PD-L1 or CTLA-4 (SLIC-2). Using a syngeneic A20 hind flank tumor model, we injected tumors with SLIC-2 or SLC-p15A-2 (equal parts mix of p15A circuit variant bacteria expressing PD-L1nb or CTLA-4nb) and monitored bacteria luminescence from the integrated $luxCDABE$ cassette in tumors over time using an in vivo imaging system (IVIS). The image sequences suggest that SLIC-2 reaches a higher bacterial luminescence than SLC-p15A-2 and that the SLC-p15A-2 strain appears to reach quorum within 24 hours (Fig. 2F). Further quantitative analysis of the images indicates that the total flux value—a proxy for the number of bacteria required for lysis—of the SLIC-2 strain is about 1.5 times greater than that of the SLC-p15A-2 strain and takes about twice as long to reach the first lysis event (Fig. 2G). These in vivo results are consistent with patterns observed in the simulations and in vitro experiments. In addition, intratumoral treatment with SLIC-2 also demonstrated a superior antitumor effect in vivo compared to SLC-p15A-2 (Fig. 2H and fig. S3). Together, our simulations provided further insight into the underlying parameters governing the dynamics and observed differences in the therapeutic efficacy of the lysis circuit variants, leading us to select SLIC as the optimal therapeutic release mechanism.

Characterizing the underlying immune response to probiotically delivered checkpoint inhibitors

After optimization of the therapeutic release mechanism, we characterized the efficacy of our therapeutic platform in an A20 lymphoma murine model, where previous literature reports antitumor effects when treated repeatedly with a combination of anti–PD-L1 and anti–CTLA-4 mAbs (31). Using a hind flank syngeneic model, we treated both flank tumors multiple times intratumorally and observed significant therapeutic efficacy in SLIC-2–treated mice compared to those treated with the control strain ($P < 0.0001$), with tumors partially or completely regressing, an increased survival benefit, and no visible hepatic metastases (Fig. 3, A to C, and fig. S4A). Consistent with literature, we also observed that some treated tumors were unresponsive to the checkpoint blockade therapy (31, 40). In mice that did not respond to the SLIC-2 treatment, no metastatic lesions were found upon ex vivo analysis, suggesting that an immune response may have been mounted to clear or prevent the formation of metastases (Fig. 3, C and D). To further understand the underlying immune response of the observed therapeutic effect, we immunophenotyped A20 tumors by flow cytometry and observed an increase in the frequency of activated CD8$^+$ T cells (CD8$^+$IFNγ^+TNFα^+) and an increase in the activation and proliferation of conventional CD4$^+$ T cells (CD4$^+$FOXP3$^-$IFNγ^+ and CD4$^+$FOXP3$^-$Ki67$^+$) in SLIC-2–treated tumors (Fig. 3, E to G). Furthermore, we observed a decrease in the frequency of regulatory T cells (CD4$^+$FOXP3$^+$) with SLIC-2 treatment (Fig. 3H). These results suggest a shift toward more responsive and less immunosuppressive T cells intratumorally, potentially resulting in

a more robust adaptive immune response and subsequently enhanced therapeutic effects in tumors treated with our engineered system.

Because multiple intratumoral injections are not ideal in a clinical setting, we explored whether a single intratumoral injection could lead to tumor regression while also controlling for the individual components of the engineered system. Subcutaneous A20-bearing mice were injected once intratumorally with either control SLIC expressing no therapeutics, SLIC expressing PD-L1nb and CTLA-4nb (SLIC-2), or the crude lysate from SLIC-2. Here, we observed significant therapeutic differences between SLIC-2 and controls ($P < 0.0001$), suggesting that strains encoding for the SLIC circuit alone, or therapeutics alone, are not effective (fig. S4B). Specifically, continuous intratumoral therapeutic production enabled by the living SLIC-2 system is essential for tumor regression. We next investigated whether a systemic immune response could be generated with a single intratumoral injection. In mice with dual flank tumors, we injected SLIC-2 into only one hind flank tumor and monitored the growth of both the treated and untreated tumors. With a single injection, we achieved a similar therapeutic effect in the treated tumor as was previously observed, with 50% of the SLIC-2–treated tumors completely regressing (Fig. 3I and fig. S4C). In the untreated tumor, we also saw a significant reduction in growth rate in the SLIC-2 group compared with single therapies ($P < 0.05$ for SLIC:CTLA-4nb; $P < 0.01$ for SLIC:PD-L1nb) and SLIC only ($P < 0.0001$), suggesting that the specific combination of PD-L1nb and CTLA-4nb induces a potent abscopal effect (Fig. 3J and fig. S4D). Immunophenotyping suggests that mice treated with SLIC-2 have increased splenic frequencies of CD44^{hi}CD62L^{hi}CD4$^+$ and CD44^{hi}CD62L^{hi}CD8$^+$ T cells, suggesting an expansion of central memory populations (Fig. 3, K and L). Together, these data support the hypothesis that a single injection of probiotically delivered checkpoint inhibitors induces a durable therapeutic response that is mediated by the adaptive immune system.

Exploration of the SLIC platform as a robust therapy

An advantage of our proposed therapeutic platform is the efficacy achieved with a single dose. Therefore, we investigated how a single injection of SLIC-2 would compare to one dose of a combination of clinically relevant anti–PD-L1 and anti–CTLA-4 mAbs. We observed a markedly enhanced effect of our probiotic system, resulting in tumor clearance and prolonged survival when compared to animals treated with the antibody combination (Fig. 4A and fig. S5A). Furthermore, 2 weeks after treatment administration, we collected serum from all animals and detected lower concentrations of systemic tumor necrosis factor α (TNFα) and an increased rate of body weight gain in SLIC-2–treated mice when compared to the nonlysing control bacteria– and antibody combination–treated mice (Fig. 4, B and C, and data file S1). This suggests the need for the lysing mechanism to control bacterial population growth and local therapeutic delivery to prevent systemic inflammation. We hypothesize that the observed therapeutic difference between the antibody and probiotic therapies is due to the probiotic's ability to continuously antagonize CTLA-4 and PD-L1 intratumorally, thereby circumventing the need for the multiple injections vital for antibody therapy success. To further interrogate the robustness of this therapeutic platform, we investigated SLIC-2 efficacy against larger, more advanced tumors. Intratumoral injection into hind flank tumors ranging from an initial volume of ~200 to 700 mm^3 resulted in either stagnated growth or complete regression of tumors, suggesting adequate bacterial colonization and maintenance of therapeutic efficacy across a broad range of tumor sizes (Fig. 4D).
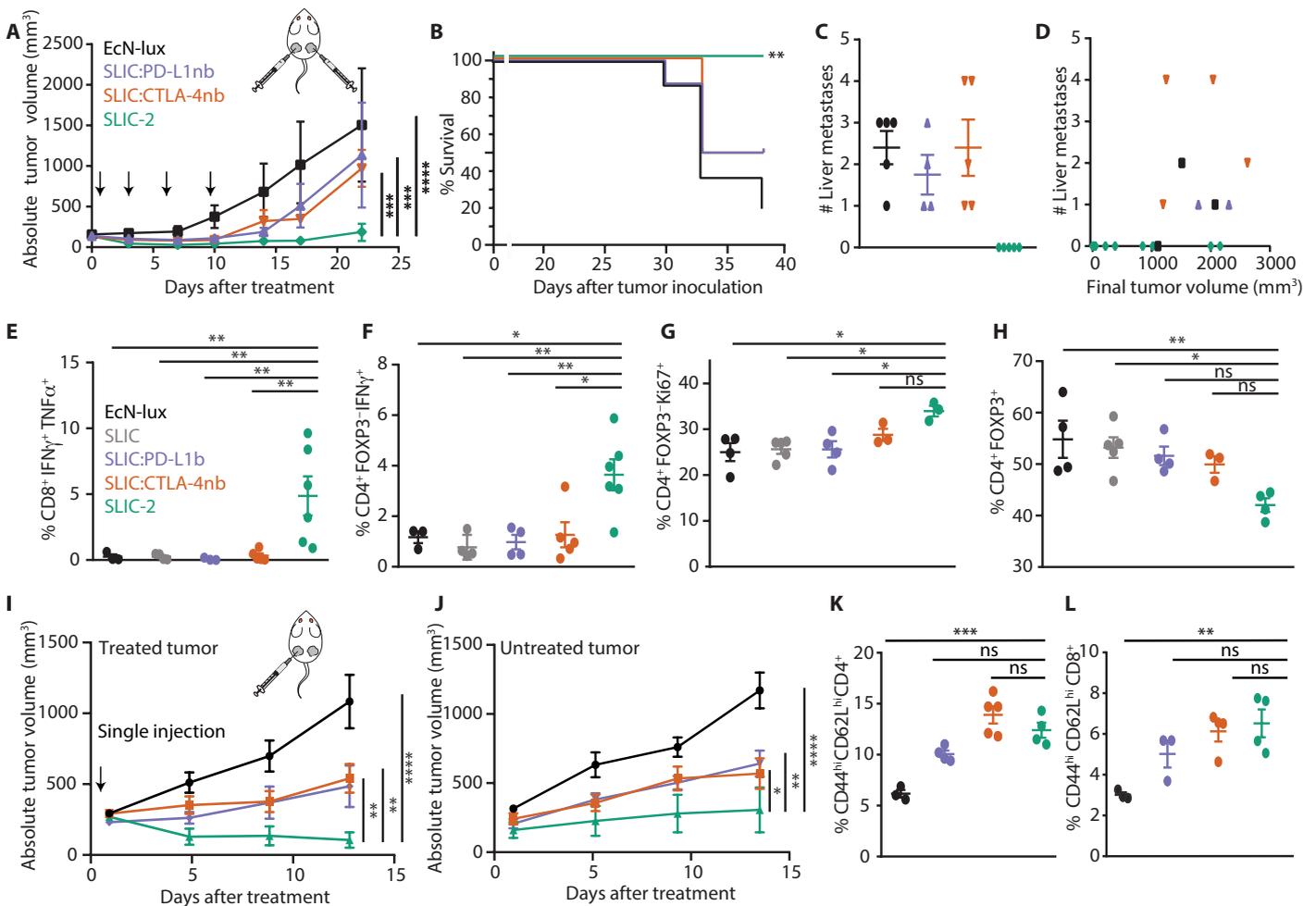
Gurbatri *et al.*, *Sci. Transl. Med.* **12**, eaax0876 (2020)   12 February 2020

4 of 12

Fig. 3. Therapeutic response to probiotically produced checkpoint inhibitors is mediated by the adaptive immune system. (A to D) BALB/c mice were implanted subcutaneously with 5×10^6 A20 cells on both hind flanks. When tumors reached ~150 to 200 mm³, mice received intratumoral injections of EcN-lux, SLIC, SLIC:CTLA-4nb, SLIC:PD-L1nb, or an equal parts combination of the latter two strains (SLIC-2) in both flanks every 3 to 4 days such that the total concentration of bacteria injected was 5×10^6 per tumor in all groups. (A) Mean absolute tumor trajectories ($n = 4$ to 7 tumors per group; two-way ANOVA with Bonferroni posttest, ***$P < 0.0005$ and ****$P < 0.0001$; error bars represent SEM of biological replicates). Individual tumor trajectories are shown in fig. S4A. (B) Survival of different treatment groups (**$P = 0.0011$, log-rank test; $n = 4$ to 5 mice per group). (C and D) Aggregated data from multiple trials showing the (C) number of visible liver metastases identified ex vivo approximately 40 days after tumor inoculation and (D) relationship between the number of liver metastases counted and the final volume of the primary tumor. (E to H) Tumor-infiltrating lymphocytes were isolated on day 8 after initial treatment and analyzed by flow cytometry for frequencies of activated (E) CD8$^+$IFNγ$^+$TNFα$^+$ and (F) CD4$^+$FOXP3$^-$IFNγ$^+$ T cells, (G) proliferating CD4$^+$FOXP3$^-$Ki67$^+$ conventional T cells, and (H) CD4$^+$FOXP3$^+$ regulatory T cells ($n = 3$ to 6 tumors per group; ordinary one-way ANOVA with Tukey's posttest, *$P < 0.05$, **$P < 0.01$; data are represented as means ± SEM of biological replicates; ns, not significant). (I and J) BALB/c mice were grafted as stated above. When tumors reached ~150 mm³, mice received a single intratumoral injection of EcN-lux, SLIC:CTLA-4nb, SLIC:PD-L1nb, or an equal parts combination of both strains (SLIC-2) into their left flank such that the total concentration of bacteria injected was 5×10^6 per tumor in all groups. Mean absolute tumor trajectories of the (I) treated tumor and (J) untreated tumor ($n = 4$ to 5 tumors per group; two-way ANOVA with Holm-Sidak posttest, *$P < 0.05$, **$P < 0.01$, ****$P < 0.0001$; error bars represent SEM of biological replicates); individual tumor trajectories are shown in fig. S4 (C and D). (K and L) Splenocytes were isolated on day 8 after initial treatment and analyzed by flow cytometry for frequencies of CD44^{hi} CD62L^{hi} central memory (K) CD4$^+$ T cells and (L) CD8$^+$ T cells ($n = 3$ to 5 tumors per group; ordinary one-way ANOVA with Tukey's posttest, ***$P < 0.001$, **$P < 0.01$; data are represented as means ± SEM of biological replicates).

Next, we sought to characterize SLIC-2 dynamics in vivo over the course of several weeks. Using IVIS imaging of bioluminescent bacterial populations, we were able to identify persistent bacterial populations within tumors, and observed sustained lysis behavior in vivo until the study's endpoint of 2 weeks after treatment (Fig. 4, E and F). To confirm the preservation of lysis dynamics, we extracted bacterial colonies from within the tumor at 3 and 14 days after treatment and tracked their growth on a plate reader. We observed nearly 100% of the plated colonies lysing at both time points (Fig. 4G),

suggesting maintenance of the integrated lysis operon and continued oscillatory behavior in vivo for multiple weeks after a single treatment. In addition, to investigate whether the bacteria remained localized, we performed biodistribution assays ex vivo and confirmed bacterial presence in only the tumor at 3 and 14 days after treatment (fig. S5B). In mice with completely regressed tumors, no bacteria were detected in peripheral organs, suggesting that the population was able to clear itself once the tumor had cleared, most likely due to the lack of necrotic core needed to sustain bacterial growth
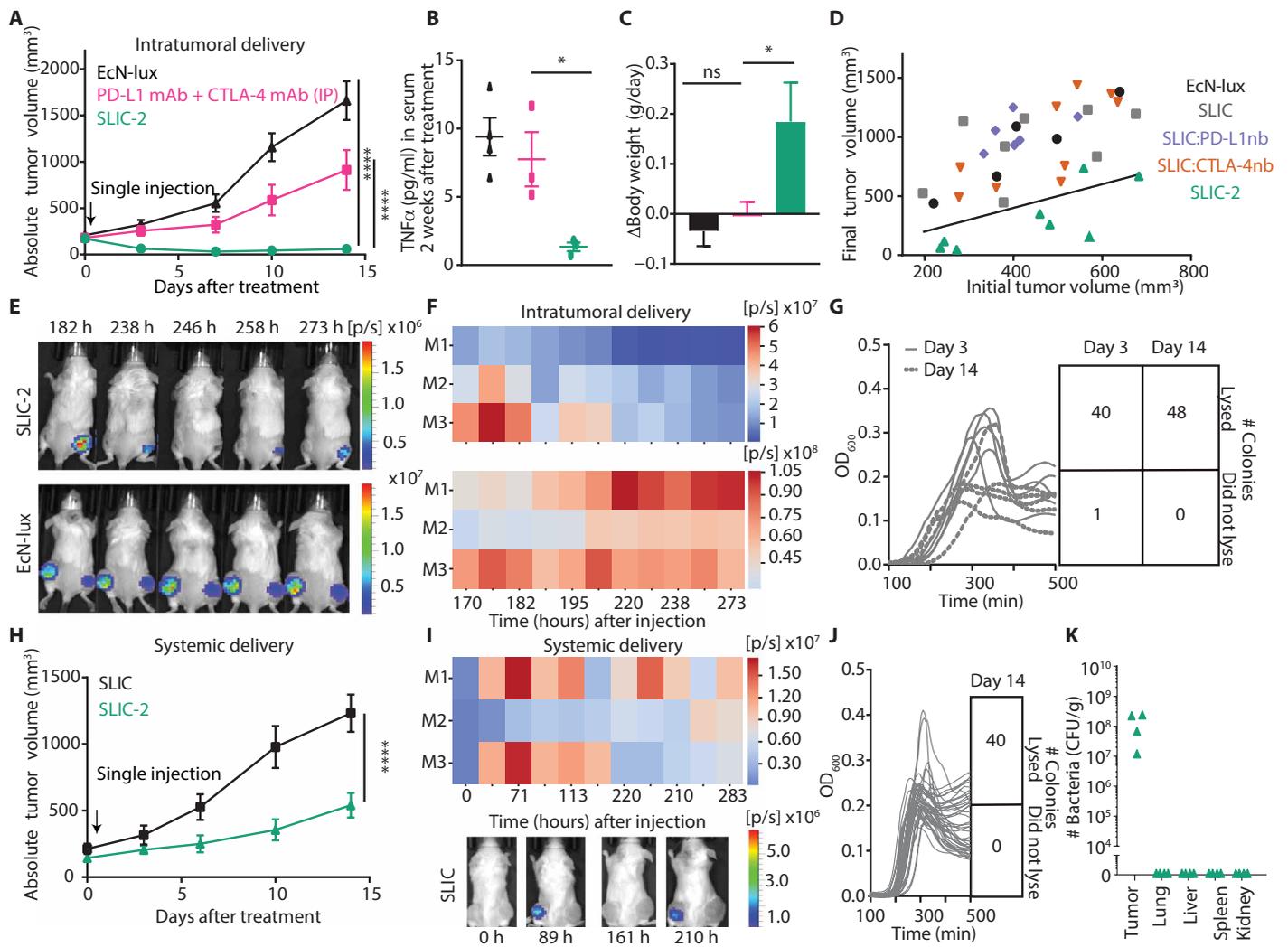
Fig. 4. Single injection of probiotics expressing checkpoint inhibitors demonstrates robustness. (**A** to **C**) BALB/c mice were implanted subcutaneously with 5×10^6 A20 cells on both hind flanks. When tumors reached ~150 to 200 mm³, mice received one intratumoral injection of EcN-lux, SLIC-2, or an intraperitoneal injection of combination of anti–PD-L1 and anti–CTLA-4 mAbs at 100 and 200 μg per mouse, respectively. (A) Mean absolute tumor trajectories (n = 8 to 10 tumors per group; two-way ANOVA with Bonferroni posttest, ****$P < 0.0001$; error bars represent SEM of biological replicates); individual tumor trajectories are shown in fig. S5A. (B) Serum concentrations of TNFα (n = 3 mice per group; ordinary one-way ANOVA with Holm-Sidak posttest, *$P = 0.0385$; data are represented as means ± SEM of biological replicates). (C) Rate of body weight gain in grams per day (n = 4 to 5 mice per group; ordinary one-way ANOVA with Tukey's posttest, *$P = 0.0387$; error bars represent SEM of biological replicates). (**D**) Scatter plot showing each tumor's final volume plotted against its initial tumor volume. Black line ($y = x$) represents the threshold where points below the line indicate tumor regression and points above the line indicate tumor growth. (**E**) Representative IVIS images of mice from the experimental groups described above, where mice were dosed once with nonlysing EcN-lux or SLIC-2. (**F**) Heatmaps quantifying total flux (photons per second) of luminescent bacteria populations over time, corresponding to IVIS images. (**G**) Plate reader experiment showing the oscillations of plated colonies from tumors harvested on days 3 and 14 after treatment and a grid showing the number of successful lysis events. (**H** to **J**) A20-bearing mice were grafted as stated above, and mice received a single intravenous injection of either 5×10^6 EcN-lux or SLIC-2 via tail vein. (H) Mean absolute tumor trajectories (n = 9 to 11 tumors per group; two-way ANOVA with Bonferroni posttest, ****$P < 0.0001$; error bars represent SEM of biological replicates). Individual tumor trajectories are shown in fig. S5D. (I) Representative IVIS images from mice treated with SLIC-2 and a heatmap quantifying the total flux (photons per second) of luminescent bacterial populations over time. (J) Plate reader experiment showing the oscillations of colonies plated from tumors harvested on day 14 after treatment and a grid of the number of successful lysis events. (**K**) Biodistribution of bacterial populations in the tumor and peripheral organs (liver, lung, spleen, and kidney) calculated as colony-forming units per gram of tissue (CFU/g).

(fig. S5B). From mice where the tumor had not completely regressed, we isolated therapeutic plasmids from the extracted bacterial colonies and confirmed that there was a lack of therapeutic plasmid loss (fig. S5C). Moreover, Sanger sequencing was used to verify the nanobody sequences, and no mutations at the nucleotide level were found.

After characterizing the therapeutic system intratumorally, we next assessed the translational potential of the system by delivering

SLIC-2 systemically. We observed that a single intravenous injection results in a significant therapeutic effect ($P < 0.0001$; Fig. 4H and fig. S5D). Similar to experiments for intratumoral delivery, we observed durable oscillations in vivo, and ex vivo analysis showed 100% of the extracted bacterial colonies lysing (Fig. 4, I and J). Furthermore, biodistribution analysis indicated that bacteria only existed within the tumor because no bacterial populations were detected in

Gurbatri *et al.*, *Sci. Transl. Med.* **12**, eaax0876 (2020)   12 February 2020

6 of 12

the lung, liver, spleen, or kidney 14 days after treatment (Fig. 4K). All mice tolerated systemic delivery of the probiotic therapy, as evidenced by the lack of decrease in mouse body weight (fig. S5E and data file S1). Together, these data suggest the efficacy, stability, and safety of the SLIC-2 platform across multiple delivery methods.

Determining the versatility of the probiotic system in an immunologically "cold" cancer

To assess the broader applicability of our approach, we tested SLIC-2 in a less immunogenic CT26 colorectal cancer model (41, 42), where immunohistochemistry (IHC) staining for CD3+ T cell populations demonstrates that CT26 tumors have fewer infiltrating T cells than A20 tumors (Fig. 5A). We performed multiple and single injections of the SLIC-2 system in subcutaneous CT26 tumors and observed a moderate, but significant ($P < 0.0001$ for multiple injection; $P < 0.005$ for single injection), therapeutic benefit (fig. S6, A and B). We hypothesized that the therapeutic effect of SLIC-2 may wane in a less immunogenic model because of minimal infiltrating T cells for the checkpoint nanobodies to engage intratumorally. As expected, when we directly compared the SLIC monotherapies to their respective mAbs, therapeutic efficacy was similar between the two therapies, and we did not see any substantial reduction in tumor growth rate, although therapy was more efficacious than the control bacteria strain (fig. S7). However, further interrogation of the underlying tumor histology indicated a higher dirty necrosis score in SLIC:PD-L1nb–treated tumors than in those treated with anti–PD-L1mAb, suggesting fewer viable tumor cells and more neutrophils present in SLIC:PD-L1nb–treated TME (Fig. 5B and fig. S8). In addition, ex vivo analysis of extracted SLIC:CTLA-4nb–treated tumors revealed a higher concentration of interferon γ (IFNγ) intratumorally (Fig. 5C), suggesting possible increased lymphocyte activation and modulation of the TME to be more amenable to treatment with other immunotherapeutic combinations.

To expand upon this system, we sought to explore combinatorial treatments to enhance antitumor activity in the CT26 model. Because of its local delivery, bacterial therapy may be used to deliver multiple therapeutics at once without increasing toxicities—a task currently difficult to achieve clinically with antibodies due to systemic toxicity (43, 44). Motivated by recent literature exploring the use of granulocyte-macrophage colony-stimulating factor (GM-CSF) as a cancer therapy, we hypothesized that GM-CSF could enhance activation of

innate immune cells, indirectly recruit T cells into the TME through enhanced antigen presentation, and ultimately cooperate with the probiotically produced checkpoint inhibitors (45–47). When we intratumorally treated both hind flanks of the syngeneic CT26 murine model with a single dose of equal parts of SLIC:PD-L1nb, SLIC:CTLA-4nb, and SLIC:GM-CSF (SLIC-3), we observed an enhanced antitumor effect when compared to the monotherapies and a greater survival benefit (Fig. 5, D and E, and fig. S9, A and B). Moreover, our dosing approach involved reducing the dose of each therapeutic strain by one-third such that the overall concentration of the bacterial combination delivered was equal across all groups in the trial. The improved therapeutic outcome suggested a useful combination of these three therapeutics that is well tolerated by mice, as was evidenced by the maintenance of health and body weight (fig. S9C and data file S1).
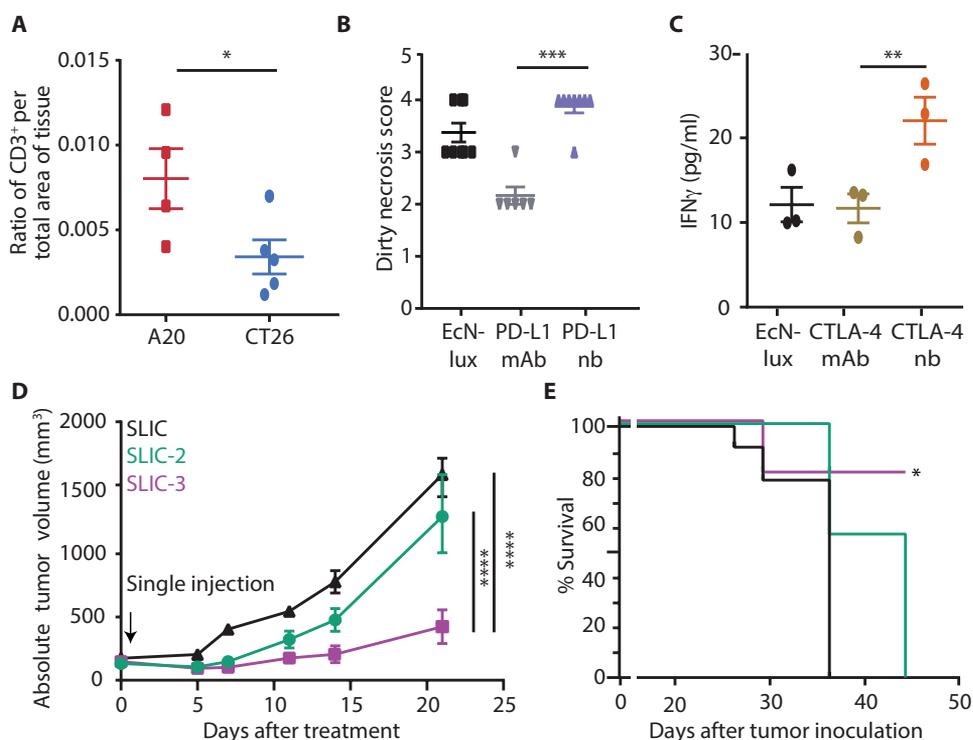

Fig. 5. The SLIC platform allows multiple therapeutics to be effectively combined for an enhanced antitumor effect in poorly immunogenic cancers. (**A**) When A20 or CT26 tumors reached ~100 to 200 mm³, mice received an intratumoral injection of PBS, and tumors were IHC stained for CD3+ populations (n = 4 to 5 tumors per group; unpaired t test, *P = 0.048; data represented as means ± SEM of biological replicates). (**B** and **C**) BALB/c mice were implanted subcutaneously with 5 × 10⁶ CT26 cells on both hind flanks. When tumors reached ~100 to 200 mm³, mice received an intratumoral injection of EcN-lux, SLIC:PD-L1nb, or SLIC:CTLA-4nb or an intraperitoneal injection of anti–PD-L1 or anti–CTLA-4 mAbs. Tumors were extracted and processed for subsequent analysis. (B) Dirty necrosis scores of tissue samples from tumors treated with EcN-lux, SLIC:PD-L1nb, or anti–PD-L1 mAb (***P = 0.007, Mann-Whitney U test; n = 6 to 8 scores per group; data represented as means ± SEM of biological replicates). (C) IFNγ concentration in SLIC:CTLA-4nb–treated tumor lysates measured by Luminex multiplex assay (n = 3 tumors per group; ordinary one-way ANOVA with Holm-Sidak posttest, *P = 0.0390; data represented as means ± SEM of biological replicates). (**D** and **E**) BALB/c mice were implanted subcutaneously with 5 × 10⁶ CT26 cells on both hind flanks. When tumors reached a volume of ~200 mm³, mice received a single intratumoral injection of SLIC, an equal parts mix of SLIC bacteria expressing PD-L1nb and CTLA-4nb (SLIC-2), or an equal parts mix of SLIC bacteria expressing PD-L1nb, CTLA-4nb, and GM-CSF (SLIC-3). (D) Mean absolute tumor trajectories (n = 5 to 6 tumors per group; one-way ANOVA with Bonferroni posttest, ****P < 0.0001; error bars represent SEM of biological replicates). Individual tumor trajectories are shown in fig. S9B. (E) Survival of different treatment groups (*P = 0.0377, log-rank test; n = 4 to 5 mice per group).

DISCUSSION

Here, we have demonstrated PD-L1 and CTLA-4 antagonists being expressed and delivered by bacteria for cancer therapy, which enabled local therapeutic production and improved antitumor activity in multiple syngeneic mouse models. Moreover, we have characterized PD-L1 and CTLA-4 nanobodies that can be adapted into other biological circuits and have optimized therapeutic release using a SLIC platform, which serves as a biocontainment measure to confine the bacterial population to the tumor site, thereby minimizing the risk of systemic toxicities.

Regarding the translational potential of our engineered probiotic platform, we have shown that a single dose delivered intratumorally or intravenously results in tumor regression. Moreover, we have demonstrated an abscopal effect, providing a potential strategy for the treatment of metastatic lesions if a primary tumor site is inaccessible for injection. One dose of our therapeutic system resulted in durable oscillations, retention of therapeutic plasmids, and clearance of bacterial population once tumors have cleared. These elements are advantageous in a clinical setting, where minimally invasive and self-sustained therapies are more desirable.

Although we explored a limited number of combination approaches, cancer immunotherapies are often more effective in combination with other anticancer agents (*48*). Microbial-based therapeutic platforms are highly modular and convenient for the rapid engineering of multiple payloads that can then be delivered as a combination of probiotic strains. Therefore, future iterations of the SLIC system can potentially be programmed to produce a wide variety of immunotherapeutics to test a variety of rational therapeutic combinations. Furthermore, we did not evaluate differences in the therapeutic effect of strains with integrated therapeutic genes versus multiple plasmid copies but hypothesize that having an increased therapeutic copy number is preferable for enhanced efficacy. In addition, our current study did not explore the mechanism by which the bacterial lysates are cleared from the body. We hypothesize that any remaining bacterial lysates in the tumor resulting from repetitive lysis are degraded by surrounding immune cells; however, further exploration into this process is necessary. Last, to make the system more clinically relevant, other routes of therapeutic administration in more translational animal models need to be considered. With this in mind, we developed the SLIC system in the probiotic strain *E. coli* Nissle 1917, which has been shown to colonize liver metastases when delivered orally (*34*), thus offering an additional translational route of therapeutic delivery for more advanced metastatic disease.

Together, we have built a stable biological circuit integrated into a probiotic with therapeutics analogous to the current treatment standard for optimization toward clinical translation. The SLIC system should help advance the cancer immunotherapy field by providing a durable delivery vehicle in which combination therapies can be easily explored, therapeutic production is sustained, and toxicities are minimized for improved checkpoint blockade delivery to a broader range of cancer patients.

MATERIALS AND METHODS
Study design

The objective of the study was to develop a probiotic platform for localized and sustainable release of checkpoint blockade nanobodies within tumors using an optimized lysis mechanism. Nanobody functionality was characterized in vitro on A20 and CT26 murine cancer cell lines. Computational modeling and subsequent in vitro and in vivo experimental validation were used to determine optimal parameters for the genetic lysis circuit. The in vivo antitumor efficacy of the probiotic platform was assessed in A20 and CT26 tumors using both intratumoral and intravenous delivery. All mice were randomized before treatment, and caliper measurements were used to track tumor volume. Mouse weight was monitored as a proxy for mouse health. Mice from varying treatment groups were either followed to generate survival curves, immunophenotyped, or imaged to visualize bacterial dynamics. Unless otherwise noted, investigators were not blinded during the study. Statistical analysis and sample sizes were determined from previous studies (*18, 23, 34*). Further details on sample size and replications (technical or biological) are provided in figure legends.

Strains and plasmids

Plasmids were constructed using Gibson assembly methods or restriction enzyme–mediated cloning methods. The copy number variant plasmids (pCG02) were constructed by cloning a geneblock (IDT) encoding a constitutively produced *luxR* and a single operon where *luxI* and ϕX174E are driven by the *luxI* promoter onto a pZS*14 plasmid backbone. The geneblock was also cloned into a pZSm46 plasmid backbone along with either the colE1 or p15A origins. For the single copy number variant, the operon was integrated into the ϕ80 site of *E. coli* Nissle 1917 using the conditional-replication, integration, and modular (CRIM) protocol (*49*). The pCG01 therapeutic plasmids were constructed by cloning a geneblock (IDT) encoding a *tac* promoter and an *E. coli* codon-optimized sequence for either the PD-L1 (RCSB PDB: 5DXW) or CTLA-4 (RCSB PDB: 5E03) nanobody with a C-terminal HA tag into a modified Axe/Txe stabilized p246-luxCDABE-AT plasmid (*33*), where the *luxCDABE* had been cloned out. pCG01 and pCG02 were transformed into electrocompetent EcN-lux. Strains were cultured in lysogeny broth (LB) medium with their respective antibiotics [sc101*variant: ampicillin (100 μg/ml); p15A variant: spectinomycin (100 μg/ml); colE1 variant: spectinomycin (100 μg/ml); and all with kanamycin (50 μg/ml) for strains transformed with pCG01] with 0.2% glucose in a 37°C shaking incubator. The protein expression plasmid was constructed by cloning a geneblock (IDT) that encoded an *E. coli* optimized sequence for either the PD-L1nb or the CTLA-4nb with a C-terminal 6× HIS tag into the multiple cloning site of a isopropyl-β-D-thiogalactopyranoside (IPTG)–inducible pET vector containing ampicillin resistance (100 μg/ml) and was transformed into NiCo21(DE3) *E. coli* (New England Biolabs).

Mammalian cells

CT26 and A20 cells were purchased from the American Type Culture Collection and cultured in RPMI 1640 (Thermo Fisher Scientific) supplemented with 10% fetal bovine serum (FBS) and 1% penicillin/streptomycin. A20 cells were grown in the same medium and additionally supplemented with 0.01% 2-mercaptoethanol. Mammalian cells were grown inside a 37°C tissue culture incubator (Thermo Fisher Scientific) maintained at 5% CO_2.

Characterization of PD-L1 and CTLA-4 nanobodies

For purification of the rCTLA-4nb and rPD-L1nb, NiCo21(DE3) *E. coli* transformed with the purification plasmid were grown at 37°C to an OD_{600} (optical density at 600 nm) of ~0.9 and induced with 1 mM IPTG for 16 hours at 30°C. Cells were then centrifuged for 10 min at 4000 relative centrifugal force (rcf) and resuspended

Gurbatri *et al.*, *Sci. Transl. Med.* **12**, eaax0876 (2020)   12 February 2020

8 of 12

in lysis buffer [50 mM NaH_2PO_4 and 300 mM NaCl (pH 8.0)]. The resuspension was then sonicated, and lysates were centrifuged for 30 min. After this, the supernatant was loaded onto Ni-NTA (Qiagen) resin, washed in wash buffer (35 mM imidazole), and eluted in 250 mM imidazole for CTLA-4nb collection or 100 mM imidazole for PD-L1nb collection. The eluates were dialyzed in phosphate-buffered saline (PBS) using regenerated cellulose dialysis tubing (3500 Da molecular weight cutoff) and then filtered through a 0.2-μm filter. Aliquots were stored at −80°C. A Bradford colorimetric assay was used to quantify purified protein.

To collect probiotically produced nanobody protein, nonlysing bacterial strains containing the PD-L1nb therapeutic plasmid were grown in a 50-ml LB culture with appropriate antibiotics to an optical density of 0.6 and then centrifuged at 3000 rcf for 5 min. The bacterial pellet was resuspended in 5 ml of RPMI medium. Samples were frozen at −80°C, thawed in a 30°C incubator five times, and centrifuged at 3000 rcf for 5 min to remove bacterial debris. The resulting lysate (1 ml) was then filtered through a 0.2-μm filter. Western blots were used for protein visualization and were probed for 1 hour with the primary anti-HA antibody (Roche) and 1 hour with a rat–horseradish peroxidase (HRP; GE Life Sciences) at room temperature. Protein was detected using a chemiluminescent substrate.

To investigate rPD-L1nb binding, 1×10^6 CT26 or A20 cells were coincubated in a 96-well V-bottom plate with a constant concentration of a fluorescently conjugated anti–PD-L1 mAb (10F.9G2 and MIH7, BioLegend) and either dilutions of the previously prepared bacterial lysate containing nanobody or the purified nanobody (rPD-L1). Quantitative comparison of the rPD-L1nb and lysate samples suggested that bacteria grown to an OD_{600} of 0.6 and mechanically lysed released ~10 μg of protein. Samples were incubated at room temperature for 2 hours, washed with ice-cold PBS, and analyzed using a BD LSRFortessa cell analyzer.

To investigate rCTLA-4nb binding, splenocytes were isolated from 6- to 8-week-old female C57BL/6 mice, and 2×10^6 splenocytes/ml were stimulated with PMA (50 ng/ml; Sigma-Aldrich) and ionomycin (1 nM, Calbiochem) and incubated at 37°C for 48 hours. Unstimulated and stimulated splenocytes were incubated with rCTLA-4nb at room temperature for 2 hours and washed with ice-cold PBS. rCTLA-4nb was detected extracellularly with an anti-HIS antibody (Qiagen), and samples were then stained intracellularly for CD3e (Tonbo) and CTLA-4 (eBioscience). All samples were analyzed using a BD LSRFortessa cell analyzer.

Animal models
All animal experiments were approved by the Institutional Animal Care and Use Committee (Columbia University, protocols AC-AAAN8002 and AC-AAAZ4470). Animals were euthanized when the tumor burden reached 2 cm in diameter or after veterinarian recommendation. Animal experiments were performed on 6- to 8-week-old female BALB/c mice (Taconic Biosciences) with bilateral subcutaneous hind flank tumors from an implanted mouse colorectal cancer cell line (CT26) or mouse B cell lymphoma line (A20). Tumor cells were prepared for implantation at a concentration of 5×10^7 cells/ml in RPMI without phenol red. Cells were implanted at 100 μl per flank, with each implant consisting of 5×10^6 cells. Unless otherwise stated, tumors were grown to an average volume of ~100 to 200 mm^3 before treatment with bacterial strains or antibodies. CT26 tumor volume was calculated by measuring the length, width, and height using calipers, where total volume = length × width × height.

Because A20 tumors are less solid, measurement of tumor z dimension is highly variable, and therefore, total volume was calculated as length × width^2 × 0.5 (50). Antibodies used for in vivo experiments included anti-mouse PD-L1 (BioXCell, catalog no. BE0101) and anti-mouse CTLA-4 (BioXCell, catalog no. BE0164), and therapeutic doses of anti–PD-L1 (100 μg per mouse) and anti–CTLA-4 (200 μg per mouse) antibodies were based on previous studies (51–53).

Therapeutic strain growth and administration
Bacterial strains were grown overnight in LB medium containing appropriate antibiotics and 0.2% glucose. The overnight culture was subcultured at a 1:100 dilution in 50 ml of fresh medium with antibiotics and glucose and grown until an OD of ~0.05 to prevent bacteria from reaching quorum. Bacteria were centrifuged at 3000 rcf for 5 min and washed three times with sterile ice-cold PBS. Bacteria were delivered intratumorally at a concentration of 5×10^8 colony-forming units (CFU)/ml in PBS with a total of 20 to 40 μl injected per flank or intravenously at a concentration of 5×10^8 CFU/ml in 100 μl of PBS.

In vivo bacterial dynamics and biodistribution
All bacterial strains used were luminescent (integrated *luxCDABE* cassette) so they could be visualized with the IVIS (34). Images were taken at multiple time points, and Living Image software was used to quantify luminescence. At the study endpoint, to assess bacterial localization, tumors, spleen, and liver were weighed and homogenized using a gentleMACS tissue dissociator (C Tubes, Miltenyi Biotec). Homogenates were serially diluted, plated on LB agar plates, and incubated overnight at 37°C. For plasmid retention analysis, tumor homogenates were also plated on LB agar plates containing kanamycin. Colonies were counted and computed as CFU per gram of tissue.

Histology
Tumors were extracted, fixed in 10% neutral buffered formalin, and sent to the Histology and Imaging Core at the University of Washington, where the tissue was processed and stained with hematoxylin and eosin or for CD3$^+$ populations. The pathologist was blinded to sample treatments and manually scored the samples for dirty necrosis (0, not present; 1, minimal; 2, mild; 3, moderate; and 4, severe, abscess like). Visiopharm software was used to calculate IHC signal.

Flow cytometry
For immunophenotyping of ex vivo tumor tissue, tumors were extracted on day 8, after bacteria treatment on days 0, 4, and 7. Lymphocytes were isolated from tumor tissue by mechanical homogenization and digestion with collagenase A (1 mg/ml; Roche) and deoxyribonuclease (DNase) I (0.5 μg/ml; Roche) in isolation buffer (RPMI 1640 supplemented with 5% FBS, 1% L-glutamine, 1% penicillin/streptomycin, and 10 mM Hepes) for 1 hour at 37°C. Cells were then filtered through 100-μm cell strainers and washed in isolation buffer before staining. A Ghost Dye cell viability stain was used as a live/dead marker. Extracellular antibodies used include anti-B220 (BD Biosciences), anti-CD4 (Tonbo), anti-CD8 (eBioscience), and anti-NKp46 (BD Biosciences). Cells were then fixed using FOXP3/transcription factor staining buffer set (Tonbo) in accordance with the manufacturer's protocol and then stained intracellularly. To measure the production of cytokines by T cells, cells were stimulated for 2 hours with PMA (50 ng/ml; Sigma-Aldrich) and ionomycin (1 nM; Calbiochem)

in the presence of brefeldin A. We stained for intracellular markers using the following antibodies: anti-TCRβ (T cell receptor β) (BD Biosciences), anti-Ki67 (Thermo Fisher Scientific), anti-TNF (eBioscience), anti-IFNγ (Tonbo), and anti-FOXP3 (eBioscience). Samples were analyzed using a BD LSRFortessa cell analyzer. FlowJo was used for all data analyses.

Mathematical model

We built upon the ordinary differential equation model explored in the original synchronized lysis circuit system (*18*). The following set of ordinary differential equations was derived to describe the bacterial population number (N; Eq. 1), total extracellular acyl homoserine lactone (AHL) molecules (H; Eq. 2), intracellular concentrations of the lysis protein (L; Eq. 3), intracellular concentrations of the LuxI protein (I; Eq. 4), and total concentration of therapeutic protein (P, Eq. 5). In this system, bacteria grow logistically at a rate of μ_N to a maximum capacity, N_0, and lyse when quorum is reached. AHL is produced at a rate proportional to bacterial population and is cleared out at a rate of μ. The lysis protein is produced at a rate proportional to copy number and is basally degraded (γ_L). The LuxI protein has similar dynamics but is further degraded by ClpXP machinery (γ_C) (*18*). The therapeutic protein production is proportional to the bacteria number and is basally degraded (γ_P) and diluted as the bacterial population grows (μ_G). Internal production of LuxI and the lysis protein is described by P_{lux} (Eq. 6), and the rate of cell degradation due to lysis is described by the hill function, γ_N (Eq. 7).

Model parameter values

To explore the dynamics of our library of lysis circuit variants, we iterated through a large range of copy numbers, with C_I and C_L ranging from 1 to 100, which is also relevant to experimental copy numbers (~1 to 70). Growth rate (μ_N) was experimentally derived, and the doubling time of ~30 min for EcN-lux was used to calculate a growth rate of 0.023 min^{-1} for computational simulations using the doubling time formula. Because growth rate and dilution due to cell growth were assumed to be equal, μ_G was set equal to μ_N. Other parameter values used include the following: α_0 (Lux promoter basal production), 0.1; α_H (Lux promoter AHL-induced production), 50; h_0 (AHL-binding affinity to Lux promoter), 5; b (AHL production rate), 20; L_0 (concentration of lysis gene resulting in half-maximum lysis), 8; n (Hill coefficient of lysis function), 2; γ_L (basal degradation of lysis protein), 1.5; K (maximum rate of cell lysis), 0.05; γ_I (basal degradation of LuxI), 5; γ_C (CLpXP degradation of LuxI), 12; N_0 (maximum cell population size), 10; γ_P (basal degradation of therapeutic protein), 2.02; and P_t (internal production of the therapeutic protein), 0.13.

$$\frac{dN}{dt} = \mu_N N \left(1 - \frac{N}{N_0}\right) - \gamma_N N \tag{1}$$

$$\frac{dH}{dt} = bNI - \frac{\mu H}{1 + \frac{N}{N_0}} \tag{2}$$

$$\frac{dL}{dt} = C_L P_{\text{lux}} - \gamma_L L - \mu_G L \tag{3}$$

$$\frac{dI}{dt} = C_I P_{\text{lux}} - \gamma_I I - \mu_G I - \gamma_C I \tag{4}$$

$$\frac{dP}{dt} = NP_\text{t} - \gamma_P P \tag{5}$$

$$P_{\text{lux}} = \alpha_0 + \frac{\alpha_H \left(\frac{H}{H_0}\right)^4}{1 + \left(\frac{H}{H_0}\right)^4} \tag{6}$$

$$\gamma_N = \frac{KL^n}{L_0^n + L^n} \tag{7}$$

Statistical analysis

Statistical tests were performed using GraphPad Prism 7.0, and the details of the statistical tests are indicated in the respective figure legends. Where data were assumed to be normally distributed, values were compared using a one-way analysis of variance (ANOVA) for a single variable or a two-way ANOVA for more than one variable, with the appropriate posttest applied for multiple comparisons. For categorical data comparisons, data were assumed to be nonparametric and a Mann-Whitney U rank test was used for single-variable, two-group comparisons. For Kaplan-Meier survival experiments, we performed a log-rank (Mantel-Cox) test.

SUPPLEMENTARY MATERIALS

stm.sciencemag.org/cgi/content/full/12/530/eaax0876/DC1

Fig. S1. Characterization of purified and probiotically produced PD-L1nb.
Fig. S2. Maps of plasmids.
Fig. S3. Individual growth trajectories of tumors treated with lysis circuit variants.
Fig. S4. Individual growth trajectories of tumors treated with different probiotic therapy regimens.
Fig. S5. Characterization of intratumorally and systemically delivered probiotic therapy.
Fig. S6. Individual tumor trajectories of multiple- and single-dose treatment regimens in a syngeneic colorectal cancer model.
Fig. S7. Tumor trajectories of probiotic and antibody therapeutics in a syngeneic colorectal cancer model.
Fig. S8. Histological images and dirty necrosis scoring in murine colorectal cancer tumors.
Fig. S9. Growth trajectories of colorectal tumors treated with SLIC-3.
Data file S1. Raw data for composite graphs.

View/request a protocol for this paper from *Bio-protocol*.

REFERENCES AND NOTES

1. T. Zhang, J. Xie, S. Arai, L. Wang, X. Shi, N. Shi, F. Ma, S. Chen, L. Huang, L. Yang, W. Ma, B. Zhang, W. Han, J. Xia, H. Chen, Y. Zhang, The efficacy and safety of anti-PD-1/PD-L1 antibodies for treatment of advanced or refractory cancers: A meta-analysis. *Oncotarget* **7**, 73068–73079 (2016).

2. S. P. D'Angelo, J. Larkin, J. A. Sosman, C. Lebbé, B. Brady, B. Neyns, H. Schmidt, J. C. Hassel, F. S. Hodi, P. Lorigan, K. J. Savage, W. H. Miller Jr., P. Mohr, I. Marquez-Rodas, J. Charles, M. Kaatz, M. Sznol, J. S. Weber, A. N. Shoushtari, M. Ruisi, J. Jiang, J. D. Wolchok, Efficacy and safety of nivolumab alone or in combination with ipilimumab in patients with mucosal melanoma: A pooled analysis. *J. Clin. Oncol.* **35**, 226–235 (2017).

3. J. Naidoo, D. B. Page, B. T. Li, L. C. Connell, K. Schindler, M. E. Lacouture, M. A. Postow, J. D. Wolchok, Toxicities of the anti-PD-1 and anti-PD-L1 immune checkpoint antibodies. *Ann. Oncol.* **26**, 2375–2391 (2015).

4. S. L. Topalian, F. S. Hodi, J. R. Brahmer, S. N. Gettinger, D. C. Smith, D. F. McDermott, J. D. Powderly, R. D. Carvajal, J. A. Sosman, M. B. Atkins, P. D. Leming, D. R. Spigel, S. J. Antonia, L. Horn, C. G. Drake, D. M. Pardoll, L. Chen, W. H. Sharfman, R. A. Anders, J. M. Taube, T. L. McMiller, H. Xu, A. J. Korman, M. Jure-Kunkel, S. Agrawal, D. McDonald, G. D. Kollia, A. Gupta, J. M. Wigginton, M. Sznol, Safety, activity, and immune correlates of anti–PD-1 antibody in cancer. *N. Eng. J. Med.* **366**, 2443–2454 (2012).

5. J. R. Brahmer, S. S. Tykodi, L. Q. Chow, W.-J. Hwu, S. L. Topalian, P. Hwu, C. G. Drake, L. H. Camacho, J. Kauh, K. Odunsi, H. C. Pitot, O. Hamid, S. Bhatia, R. Martins, K. Eaton, S. Chen, T. M. Salay, S. Alaparthy, J. F. Grosso, A. J. Korman, S. M. Parker, S. Agrawal, S. M. Goldberg, D. M. Pardoll, A. Gupta, J. M. Wigginton, Safety and activity of anti–PD-L1 antibody in patients with advanced cancer. *N. Engl. J. Med.* **366**, 2455–2465 (2012).

6. J. Michot, C. Bigenwald, S. Champiat, M. Collins, F. Carbonnel, S. Postel-Vinay, A. Berdelou, A. Varga, R. Bahleda, A. Hollebecque, C. Massard, A. Fuerea, V. Ribrag, A. Gazzah, J. P. Armand, N. Amellal, E. Angevin, N. Noel, C. Boutros, C. Mateus, C. Robert, J. C. Soria, A. Marabelle, O. Lambotte, Immune-related adverse events with immune checkpoint blockade: A comprehensive review. *Eur. J. Cancer* **54**, 139–148 (2016).

7. Y. K. Chae, A. Arya, W. Iams, M. R. Cruz, S. Chandra, J. Choi, F. Giles, Current landscape and future of dual anti-CTLA4 and PD-1/PD-L1 blockade immunotherapy in cancer; lessons learned from clinical trials with melanoma and non-small cell lung cancer (NSCLC). *J. Immunother. Cancer* **6**, 39 (2018).

8. X. Du, M. Liu, J. Su, P. Zhang, F. Tang, P. Ye, M. Devenport, X. Wang, Y. Zhang, Y. Liu, P. Zheng, Uncoupling therapeutic from immunotherapy-related adverse effects for safer and effective anti-CTLA-4 antibodies in CTLA4 humanized mice. *Cell Res.* **28**, 433–447 (2018).

9. T. S. Gardner, C. R. Cantor, J. J. Collins, Construction of a genetic toggle switch in Escherichia coli. *Nature* **403**, 339–342 (2000).

10. M. B. Elowitz, S. Leibler, A synthetic oscillatory network of transcriptional regulators. *Nature* **403**, 335–338 (2000).

11. J. Stricker, S. Cookson, M. R. Bennett, W. H. Mather, L. S. Tsimring, J. Hasty, A fast, robust and tunable synthetic gene oscillator. *Nature* **456**, 516–519 (2008).

12. T. Danino, O. Mondragón-Palomino, L. Tsimring, J. Hasty, A synchronized quorum of genetic clocks. *Nature* **463**, 326–330 (2010).

13. A. Prindle, P. Samayoa, I. Razinkov, T. Danino, L. S. Tsimring, J. Hasty, A sensing array of radically coupled genetic 'biopixels'. *Nature* **481**, 39–44 (2012).

14. J. J. Tabor, H. M. Salis, Z. B. Simpson, A. A. Chevalier, A. Levskaya, E. M. Marcotte, C. A. Voigt, A. D. Ellington, A synthetic genetic edge detection program. *Cell* **137**, 1272–1281 (2009).

15. C. Liu, X. Fu, L. Liu, X. Ren, C. K. Chau, S. Li, L. Xiang, H. Zeng, G. Chen, L.-H. Tang, P. Lenz, X. Cui, W. Huang, T. Hwa, J.-D. Huang, Sequential establishment of stripe patterns in an expanding cell population. *Science* **334**, 238–241 (2011).

16. D. T. Riglar, D. L. Richmond, L. Potvin-Trottier, A. A. Verdegaal, A. D. Naydich, S. Bakshi, E. Leoncini, L. G. Lyon, J. Paulsson, P. A. Silver, Bacterial variability in the mammalian gut captured by a single-cell synthetic oscillator. *Nat. Commun.* **10**, 1–12 (2019).

17. I. Y. Hwang, E. Koh, A. Wong, J. C. March, W. E. Bentley, Y. S. Lee, M. W. Chang, Engineered probiotic Escherichia coli can eliminate and prevent Pseudomonas aeruginosa gut infection in animal models. *Nat. Commun.* **8**, 15028 (2017).

18. M. O. Din, T. Danino, A. Prindle, M. Skalak, J. Selimkhanov, K. Allen, E. Julio, E. Atolia, L. S. Tsimring, S. N. Bhatia, J. Hasty, Synchronized cycles of bacterial lysis for in vivo delivery. *Nature* **536**, 81–85 (2016).

19. J. H. Zheng, V. H. Nguyen, S.-N. Jiang, S.-H. Park, W. Tan, S. H. Hong, M. G. Shin, I.-J. Chung, Y. Hong, H.-S. Bom, H. E. Choy, S. E. Lee, J. H. Rhee, J.-J. Min, Two-step enhanced cancer immunotherapy with engineered *Salmonella typhimurium* secreting heterologous flagellin. *Sci. Transl. Med.* **9**, eaak9537 (2017).

20. J. C. Anderson, E. J. Clarke, A. P. Arkin, C. A. Voigt, Environmentally controlled invasion of cancer cells by engineered bacteria. *J. Mol. Biol.* **355**, 619–627 (2006).

21. S. Leschner, K. Westphal, N. Dietrich, N. Viegas, J. Jablonska, M. Lyszkiewicz, S. Lienenklaus, W. Falk, N. Gekara, H. Loessner, S. Weiss, Tumor invasion of Salmonella enterica serovar Typhimurium is accompanied by strong hemorrhage promoted by TNF-α. *PLOS ONE* **4**, e6692 (2009).

22. N. S. Forbes, Engineering the perfect (bacterial) cancer therapy. *Nat. Rev. Cancer* **10**, 785–794 (2010).

23. T. Danino, J. Lo, A. Prindle, J. Hasty, S. N. Bhatia, In vivo gene expression dynamics of tumor-targeted bacteria. *ACS Synth. Biol.* **1**, 465–470 (2012).

24. M. Zhao, M. Yang, X.-M. Li, P. Jiang, E. Baranov, S. Li, M. Xu, S. Penman, R. M. Hoffman, Tumor-targeting bacterial therapy with amino acid auxotrophs of GFP-expressing *Salmonella typhimurium*. *Proc. Natl. Acad. Sci. U.S.A.* **102**, 755–760 (2005).

25. S. Zhou, C. Gravekamp, D. Bermudes, K. Liu, Tumour-targeting bacteria engineered to fight cancer. *Nat. Rev. Cancer* **1**, 727–743 (2018).

26. R. D. Berg, The indigenous gastrointestinal microflora. *Trends Microbiol.* **4**, 430–435 (1996).

27. D. C. Savage, Microorganisms associated with epithelial surfaces and stability of the indigenous gastrointestinal microflora. *Mol. Nutr. Food Res.* **31**, 383–395 (1987).

28. P. Bannas, J. Hambach, F. Koch-Nolte, Nanobodies and nanobody-based human heavy chain antibodies as antitumor therapeutics. *Front. Immunol.* **8**, 1603 (2017).

29. Y. J. Lee, K. J. Jeong, Challenges to production of antibodies in bacteria and yeast. *J. Biosci. Bioeng.* **120**, 483–490 (2015).

30. Y. Hu, C. Liu, S. Muyldermans, Nanobody-based delivery systems for diagnosis and targeted tumor therapy. *Front. Immunol.* **8**, 1442 (2017).

31. I. Sagiv-Barfi, H. E. Kohrt, D. K. Czerwinski, P. P. Ng, B. Y. Chang, R. Levy, Therapeutic antitumor immunity by checkpoint blockade is enhanced by ibrutinib, an inhibitor of both BTK and ITK. *Proc. Natl. Acad. Sci. U.S.A.* **112**, E966–E972 (2015).

32. K. Kim, A. Skora, Z. Li, A. Tam, L. Diaz, N. Papadopolous, L. Blosser, K. Kinzler, B. Vogelstein, S. Zhou, Eradication of metastatic mouse cancers resistant to immune checkpoint blockade by suppression of myeloid-derived cells. *J. Immunother. Cancer* **2**, P267 (2014).

33. A. J. H. Fedorec, T. Ozdemir, A. Doshi, L. Rosa, O. Velazquez, T. Danino, C. P. Barnes, Two new plasmid post-segregational killing mechanisms for the implementation of synthetic gene networks in *Escherichia coli*. *Science* **14**, 323–334 (2019).

34. T. Danino, A. Prindle, G. A. Kwong, M. Skalak, H. Li, K. Allen, J. Hasty, S. N. Bhatia, Programmable probiotics for detection of cancer in urine. *Sci. Transl. Med.* **7**, 289ra84 (2015).

35. Y. Zhang, Y. Zhang, L. Xia, X. Zhang, X. Ding, F. Yan, F. Wu, *Escherichia coli* Nissle 1917 targets and restrains mouse B16 melanoma and 4T1 breast tumors through expression of azurin protein. *Appl. Environ. Microbiol.* **78**, 7603–7610 (2012).

36. L. He, H. Yang, J. Tang, Z. Liu, Y. Chen, B. Lu, H. He, S. Tang, Y. Sun, F. Liu, Intestinal probiotics *E. coli* Nissle 1917 as a targeted vehicle for delivery of p53 and Tum-5 to solid tumors for cancer therapy. *J. Biol. Eng.* **13**, 58 (2019).

37. T. Secher, S. Kassem, M. Benamar, I. Bernard, M. Boury, F. Barreau, E. Oswald, A. Saoudi, Oral administration of the probiotic strain Escherichia coli Nissle 1917 reduces susceptibility to neuroinflammation and repairs experimental autoimmune encephalomyelitis-induced intestinal barrier dysfunction. *Front. Immunol.* **8**, 1096 (2017).

38. V. V. Ganusov, A. V. Brilkov, Estimating the instability parameters of plasmid-bearing cells. I. Chemostat culture. *J. Theor. Biol.* **219**, 193–205 (2002).

39. L. Boe, Estimation of plasmid loss rates in bacterial populations with a reference to the reproducibility of stability experiments. *Plasmid* **36**, 161–167 (1996).

40. J. Rios-Doria, N. Durham, L. Wetzel, R. Rothstein, J. Chesebrough, N. Holoweckyj, W. Zhao, C. C. Leow, R. Hollingsworth, Doxil synergizes with cancer immunotherapies to enhance antitumor responses in syngeneic mouse models. *Neoplasia* **17**, 661–670 (2015).

41. B. W. Sandage, J. J. Talley, E. J. Martinez, M. R. Franklin, M. A. Meade, D. Saims, M. Thayer, S. Wise, D. Draper, W. Leopold, Abstract 2619: Combination of ECP1014 and anti-PD-L1 reduces tumor growth in the CT26 murine colon carcinoma model of a cold tumor. *Cancer Res.* **77**, 2619 (2017).

42. E. R. Fearon, D. M. Pardoll, T. Itaya, P. Golumbek, H. I. Levitsky, J. W. Simons, H. Karasuyama, B. Vogelstein, P. Frost, Interleukin-2 production by tumor cells bypasses T helper function in the generation of an antitumor response. *Cell* **60**, 397–403 (1990).

43. F. Kroschinsky, F. Stölzel, S. von Bonin, G. Beutel, M. Kochanek, M. Kiehl, P. Schellongowski; Intensive Care in Hematological and Oncological Patients (iCHOP) Collaborative Group, New drugs, new toxicities: Severe side effects of modern targeted and immunotherapy of cancer and their management. *Crit. Care* **21**, 89 (2017).

44. I. Corraliza-Gorjón, B. Somovilla-Crespo, S. Santamaria, J. A. Garcia-Sanz, L. Kremer, New strategies using antibody combinations to increase cancer treatment effectiveness. *Front. Immunol.* **8**, 1804 (2017).

45. F. S. Hodi, S. Lee, D. F. McDermott, U. N. Rao, L. H. Butterfield, A. A. Tarhini, P. Leming, I. Puzanov, D. Shin, J. M. Kirkwood, Ipilimumab plus sargramostim vs ipilimumab alone for treatment of metastatic melanoma: A randomized clinical trial. *JAMA* **312**, 1744–1753 (2014).

46. E. J. Small, D. M. Reese, B. Um, S. Whisenant, S. C. Dixon, W. D. Figg, Therapy of advanced prostate cancer with granulocyte macrophage colony-stimulating factor. *Clin. Cancer Res.* **5**, 1738–1744 (1999).

47. J. J. Everly, S. Lonial, Immunomodulatory effects of human recombinant granulocyte-macrophage colony-stimulating factor (rhuGM-CSF): Evidence of antitumour activity. *Expert Opin. Biol. Ther.* **5**, 293–311 (2005).

48. E. V. Schmidt, Developing combination strategies using PD-1 checkpoint inhibitors to treat cancer. *Sem. Immunopathol.* **41**, 21–30 (2019).

49. A. Haldimann, B. L. Wanner, Conditional-replication, integration, excision, and retrieval plasmid-host systems for gene structure-function studies of bacteria. *J. Bacteriol.* **183**, 6384–6393 (2001).

50. X. Liu, Y. Pu, K. Cron, L. Deng, J. Kline, W. A. Frazier, H. Xu, H. Peng, Y.-X. Fu, M. M. Xu, CD47 blockade triggers T cell–mediated destruction of immunogenic tumors. *Nat. Med.* **21**, 1209–1215 (2015).

51. W. L. Redmond, S. N. Linch, M. J. Kasiewicz, Combined targeting of costimulatory (OX40) and coinhibitory (CTLA-4) pathways elicits potent effector T cells capable of driving robust antitumor immunity. *Cancer Immunol. Res.* **2**, 142–153 (2014).

52. M. J. Selby, J. J. Engelhardt, M. Quigley, K. A. Henning, T. Chen, M. Srinivasan, A. J. Korman, Anti-CTLA-4 antibodies of IgG2a isotype enhance antitumor activity through reduction of intratumoral regulatory T cells. *Cancer Immunol. Res.* **1**, 32–42 (2013).

53. F. T. H. Wu, P. Xu, A. Chow, S. Man, J. Krüger, K. A. Khan, M. Paez-Ribes, E. Pham, R. S. Kerbel, Pre- and post-operative anti-PD-L1 plus anti-angiogenic therapies in mouse breast or renal cancer models of micro- or macro-metastatic disease. *Br. J. Cancer* **120**, 196–206 (2019).

Citation: C. R. Gurbatri, I. Lia, R. Vincent, C. Coker, S. Castro, P. M. Treuting, T. E. Hinchliffe, N. Arpaia, T. Danino, Engineered probiotics for local tumor delivery of checkpoint blockade nanobodies. *Sci. Transl. Med.* **12**, eaax0876 (2020).

Gurbatri *et al.*, *Sci. Transl. Med.* **12**, eaax0876 (2020) 12 February 2020

12 of 12

Science Translational Medicine

Engineered probiotics for local tumor delivery of checkpoint blockade nanobodies

Candice R. Gurbatri, Ioana Lia, Rosa Vincent, Courtney Coker, Samuel Castro, Piper M. Treuting, Taylor E. Hinchliffe, Nicholas Arpaia and Tal Danino

Bacterial helpers to the rescue

Immune checkpoint inhibitors are a promising and increasingly popular approach to cancer therapy. Unfortunately, they sometimes have severe immune-mediated side effects, which can be minimized by local delivery of immunotherapy to the tumors. To address this problem, Gurbatri *et al.* engineered a probiotic bacteria system to release nanobodies targeting the immune checkpoints. After the bacteria were injected into a tumor, they stimulated a systemic antitumor immune response, successfully attacking not only the injected tumor but also any others found in the body. They could also be engineered to express an immunostimulatory cytokine to further boost the antitumor response in less immunogenic tumors.

ARTICLE TOOLS	http://stm.sciencemag.org/content/12/530/eaax0876
SUPPLEMENTARY MATERIALS	http://stm.sciencemag.org/content/suppl/2020/02/10/12.530.eaax0876.DC1
RELATED CONTENT	http://stm.sciencemag.org/content/scitransmed/12/526/eaax7992.full http://stm.sciencemag.org/content/scitransmed/11/477/eaat7973.full http://stm.sciencemag.org/content/scitransmed/10/429/eaan3682.full http://stm.sciencemag.org/content/scitransmed/9/415/eaan0401.full http://stm.sciencemag.org/content/scitransmed/12/534/eaav7431.full http://science.sciencemag.org/content/sci/368/6494/938.full http://science.sciencemag.org/content/sci/368/6494/973.full http://stm.sciencemag.org/content/scitransmed/12/548/eaav9760.full http://science.sciencemag.org/content/sci/369/6510/1427.full http://science.sciencemag.org/content/sci/369/6510/1481.full http://stm.sciencemag.org/content/scitransmed/12/563/eaay3575.full http://stm.sciencemag.org/content/scitransmed/12/567/eaax4905.full http://science.sciencemag.org/content/sci/371/6529/602.full http://science.sciencemag.org/content/sci/371/6529/573.full http://science.sciencemag.org/content/sci/371/6529/595.full http://science.sciencemag.org/content/sci/371/6536/eabc4552.full
REFERENCES	This article cites 53 articles, 12 of which you can access for free http://stm.sciencemag.org/content/12/530/eaax0876#BIBL
PERMISSIONS	http://www.sciencemag.org/help/reprints-and-permissions

Use of this article is subject to the Terms of Service